AGU PUBLICATIONS

JGR

Journal of Geophysical Research: Solid Earth

RESEARCH ARTICLE
10.1002/2015JB012713

Key Points:
- Damage fault zones could promote the rupture extents
- The promotional effects increase with the width and depth extent of damage fault zones
- Along-strike segmented fault zones may lead to preferred rupture directions

Correspondence to:
H. Yang,
hyang@cuhk.edu.hk

Citation:
Weng, H., H. Yang, Z. Zhang, and X. Chen (2016), Earthquake rupture extents and coseismic slips promoted by damaged fault zones, *J. Geophys. Res. Solid Earth*, *121*, doi:10.1002/2015JB012713.

Received 3 DEC 2015
Accepted 16 MAY 2016
Accepted article online 20 MAY 2016

©2016. American Geophysical Union. All Rights Reserved.

Earthquake rupture extents and coseismic slips promoted by damaged fault zones

Huihui Weng[1], Hongfeng Yang[1], Zhenguo Zhang[2], and Xiaofei Chen[2]

[1]Earth System Science Programme, Faculty of Science, Chinese University of Hong Kong, Hong Kong, [2]School of Earth and Space Sciences, University of Science and Technology of China, Hefei, China

Abstract Here we investigate the effects of damage fault zones on rupture propagation by conducting a series of 3-D dynamic rupture simulations on a planar vertical strike-slip fault. We find that damage fault zones can promote rupture extent and increase earthquake potency. The waves reflected from the bottom of shallow damage fault zones can increase shear stress on the fault and thus promote rupture propagation. In addition, the promotional effects increase with the width and depth extent of damage fault zones. The overall effects of the waves reflected from the fault-parallel side boundaries of damage fault zones are unfavorable for rupture propagation. Therefore, rupture propagation is promoted with the increased width of fault zones due to geometrical spreading effects. Moreover, nonground-breaking ruptures may reach the ground surface with the effects of damage fault zones. Furthermore, along-strike segmented fault zones as suggested by observations could also promote ruptures and may lead to preferred rupture directions if epicenters are close to fault zones. The effects of damage fault zones on rupture propagation hold important implications on assessing earthquake risk.

1. Introduction

Damaged zones are often found surrounding crustal faults and are termed low-velocity fault zones (LVFZs) due to significantly reduced seismic velocities compared to the host rock [e.g., *Ben-Zion et al.*, 2003; *Ben-Zion and Huang*, 2002; *Cochran et al.*, 2009; *Lewis and Ben-Zion*, 2010; *Li et al.*, 2007; *Li et al.*, 2002; *Li and Vernon*, 2001; *Mizuno et al.*, 2008; *Yang et al.*, 2014; *Yang and Zhu*, 2010; *Yang et al.*, 2011]. LVFZs may result in asymmetric damage patterns during past earthquakes [e.g., *Ben-Zion and Sammis*, 2003; *Dor et al.*, 2006], amplify ground motion [e.g., *Ben-Zion and Aki*, 1990], and modulate rupture propagation [e.g., *Huang and Ampuero*, 2011; *Huang et al.*, 2014]. Understanding the development of damage zones and their effects on earthquake ruptures is of significant importance to better understand earthquake physics.

It has been widely shown that LVFZs, as well as other heterogeneities on the fault, may significantly affect earthquake rupture propagation [*Brietzke and Ben-Zion*, 2006; *Harris and Day*, 1997; *Huang and Ampuero*, 2011; *Huang et al.*, 2014; *Pelties et al.*, 2015; *Weng et al.*, 2015; *Yang et al.*, 2013], earthquake nucleation [*Ampuero et al.*, 2002], and earthquake cycle properties [*Kaneko et al.*, 2011; *Yang et al.*, 2012]. For instance, it has been suggested that LVFZs could produce pulse-like ruptures if their velocity reduction is sufficiently large [*Huang and Ampuero*, 2011; *Huang et al.*, 2014]. In addition, LVFZs may also cause transient supershear ruptures in a 2-D model [e.g., *Huang et al.*, 2014, 2016; *Ma and Elbanna*, 2015]. By conducting dynamic rupture simulations in 3-D models, pulse-like ruptures are also found due to the effects of the LVFZ [e.g., *Pelties et al.*, 2015]. Furthermore, LVFZs may cause significant ground deformation in response to neighboring earthquakes [*Kang and Duan*, 2015; *Fialko*, 2004].

While these investigations significantly advance our understanding of the effects of LVFZs on rupture propagation and ground deformations during earthquakes, they also underscore the importance of detailed investigations of how other important factors of LVFZs, such as their depth extent and along-strike variation, may modulate earthquake ruptures [e.g., *Pelties et al.*, 2015; *Cappa et al.*, 2014; *Yang*, 2015]. In this work we conduct 3-D dynamic rupture simulations to better understand the effects of LVFZs on rupture propagation. We find that LVFZs can promote rupture extent and increase earthquake potency. Such findings hold important implications for earthquake hazard assessment, especially for regions where low-velocity fault zones and sedimentary basins are identified.

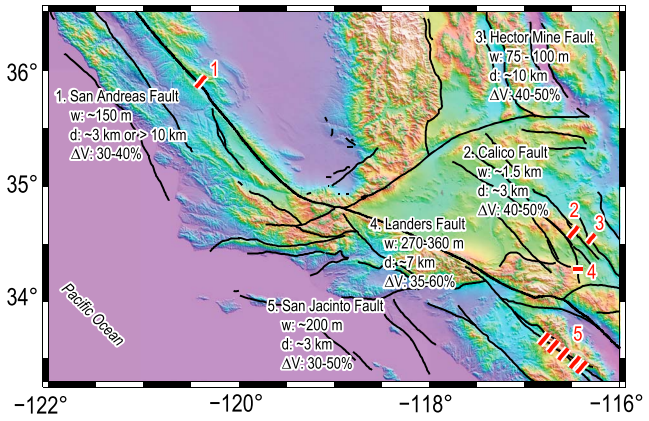

Figure 1. Observed low-velocity fault zones in California (red bars). Black lines indicate faults in the region. *d*, *w*, and Δ*V* mark the depth extent, the width, and the velocity reduction of the fault zones.

2. LVFZ Observations

A number of investigations have been conducted to probe the properties of LVFZs, such as fault zone waves, earthquake location, ambient noise cross correlation, gravity, interferometric synthetic aperture radar, and GPS data [e.g., *Ben-Zion et al.*, 2003; *Cochran et al.*, 2009; *Hillers et al.*, 2014; *Lewis et al.*, 2005; *Lewis and Ben-Zion*, 2010; *Li et al.*, 2007, 2002; *Li and Vernon*, 2001; *Lindsey et al.*, 2014; *Mizuno et al.*, 2008; *Stierman*, 1984; *Yang et al.*, 2014; *Yang and Zhu*, 2010; *Yang et al.*, 2011; *Huang et al.*, 2016]. In general, the width and velocity reduction of the LVFZ are well constrained, ranging from hundreds to thousands of meters and 20–60%, respectively. For instance, the Calico fault in the East California Shear Zone has been suggested to have a LVFZ with a width of ~1.5 km and velocity reduction of 40–50% relative to the host rock (Figure 1) [*Cochran et al.*, 2009; *Yang et al.*, 2011]. The Landers fault is thought to have a LVFZ with a width of 270–360 m and 35–60% velocity reduction in *P* and *S* velocities [*Li et al.*, 2007, 1994; *Peng et al.*, 2003]. However, the depth extent of the LVFZ has been in debate. For instance, the San Andreas fault (SAF) near Parkfield is suggested to host a LVFZ extending to a depth of ~3 km from a comprehensive analysis of fault zone trapped waves [e.g., *Lewis and Ben-Zion*, 2010]. In contrast, this LVFZ has also been suggested to extend to a depth of ~10 km or greater from analysis of differential group velocity using the two-station technique [e.g., *Wu et al.*, 2010].

In addition to the width, depth extent, and velocity reduction relative to the host rock, along-strike variations of LVFZ properties have also been documented using different techniques [e.g., *Lewis and Ben-Zion*, 2010; *Allam et al.*, 2014; *Yang et al.*, 2014]. For instance, prominent LVFZs are found beneath three out of five small-aperture temporary arrays across the San Jacinto fault (SJF) in Southern California [*Yang et al.*, 2014], indicating clear along-strike variations that are consistent with the results from regional seismic tomographic images [*Allam et al.*, 2014]. Similar along-strike variation of shallow trapping structure has also been found along the SAF near Parkfield [*Lewis and Ben-Zion*, 2010]. Recent numerical simulations with along-strike variations in the elastic modulus of the long-term damage zone successfully predict the observed generic, triangular envelope shape of natural coseismic slip profiles [*Cappa et al.*, 2014], suggesting significant inelastic deformation near the faults during earthquakes.

3. Numerical Models

3.1. Fault Dimension and LVFZ Properties

Here we build up a 3-D model with a strike-slip fault bisecting the domain (Figure 2). The fault model is set analogously to the SJF for the following reasons. First, the LVFZs along the SJF are well documented [e.g., *Li and Vernon*, 2001; *Lewis et al.*, 2005; *Yang and Zhu*, 2010; *Yang et al.*, 2014]. Second, the seismogenic zone of the SJF is well delineated by seismicity. For instance, local seismicity extends approximately to 10 km depth in the southern SJF [*Wdowinski*, 2009]. Our model domain is $24 \times 40 \times 16\ \mathrm{km}^3$ (Table 1). The fault plane extends 36 km in length and 10 km in depth. We set the seismogenic depth as 3–10 km since we focus on nonground-breaking earthquakes. In a few cases, we also allow ruptures propagate to the free surface by setting the seismogenic zone from 0 to 10 km.

In this study we consider ranges of LVFZ parameters that cover the observations and extend to larger parameter spaces to provide more insights into earthquake physics. We define the geometries of the LVFZ by the width *w*, the depth extent *d*, and the relative velocity reduction of both *P* wave and *S* wave velocities $\Delta V = 1 - V_{\mathrm{LVFZ}}/V_{\mathrm{host\ rock}}$ (Figure 2). *w* is changed from 0 km to 5 km, *d* is changed from 0 km to 10 km, and Δ*V* varies from 0% to 40%. In addition, we also consider the effects of along-strike variations of the LVFZ by changing its along-strike length. To focus on the effects of LVFZs on rupture propagation, the material

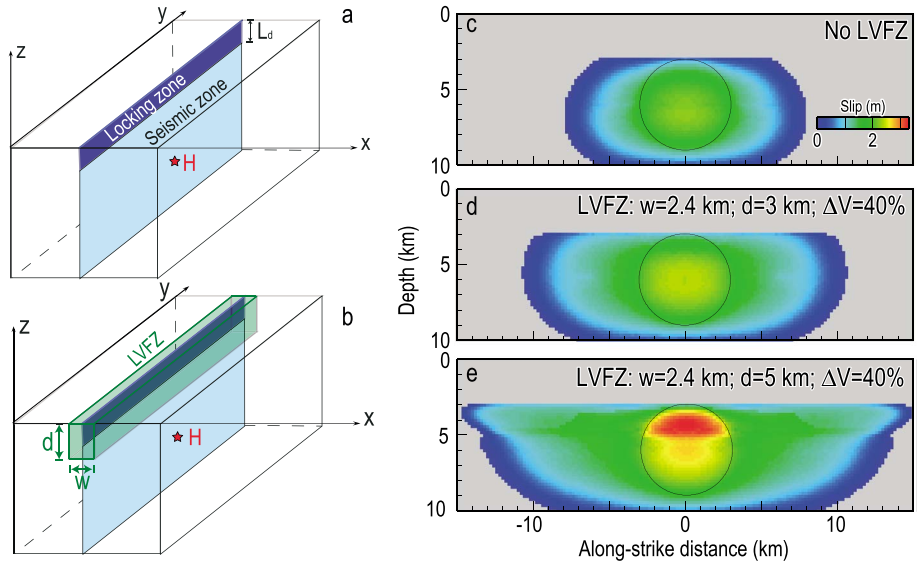

Figure 2. (a) Model setup of 3-D dynamic rupture simulation with homogeneous material. Blue rectangle marks the aseismic region with a depth extent of L_d. Light blue rectangle marks the seismogenic zone. Red star marks the hypocenter. (b) A low-velocity zone (LVFZ) is shown as the light green box. *w* and *d* indicate the width and depth extent of the LVFZ. (c–e) Coseismic slip distribution (color) for models without LVFZ (Figure 2c), with a LVFZ (Figures 2d and 2e). Circles mark the nucleation zones.

properties of host rock are kept constant for all the simulated models: $\rho = 2760$ kg/m^3, $V_P = 5.77$ km/s, $V_S = 3.33$ km/s, shear modulus $\mu = 30$ GPa, and Poisson's ratio $\nu = 0.25$ (Figure 2).

3.2. Dynamic Rupture Simulations

We simulate 3-D dynamic rupture scenarios using a finite element code, PyLith [*Aagaard et al.*, 2013]. A linear slip-weakening friction law is applied on the fault [*Ida*, 1972], in which the friction coefficient f linearly decreases from its static value f_s to dynamic value f_d over a characteristic slip d_0:

$$f(\delta) = \begin{cases} f_s - (f_s - f_d)\delta/d_0 & \delta \le d_0 \\ f_d & \delta > d_0 \end{cases} \quad (1)$$

where f_s is the static friction coefficient, f_d is the dynamic friction coefficient, δ is fault slip, and d_0 is the characteristic slip-weakening distance. In this study we choose a uniform ambient effective normal stress for simplicity (i.e., $\sigma_n = 100$ MPa). f_s, f_d, d_0, and τ_0 are all uniform on the fault (Table 1). Absorbing boundaries are applied on all sides of the domain except for the free surface.

We introduce a circular nucleation zone, whose initial shear stress is slightly above the static friction strength (Table 1) and whose radius is chosen such that the rupture could initiate inside the nucleation zone and propagate outward on the fault, governed by the slip-weakening law. It has been shown that 3-D ruptures could stop spontaneously, rupturing a small region if the size of the nucleation patch is smaller than a threshold [*Galis et al.*, 2015; *Xu et al.*, 2015]. On an unbounded fault, the critical nucleation size can be estimated using the following equation

$$R_{\text{nuc}} = \frac{\pi}{4}\frac{1}{F_{\text{min}}^2}\frac{\tau_s - \tau_d}{(\tau_0 - \tau_d)^2}\mu d_0 \quad (2)$$

where R_{nuc} is the critical nucleation radius, τ_0, τ_s and τ_d are initial shear stress, static, and dynamic shear stresses, respectively [*Galis et al.*, 2015]. $\tau_s = \sigma_n f_s$ and $\tau_d = \sigma_n f_d$. F_{min} is a minimum of the function

$$F(x) = \sqrt{x}\left[1 + \frac{\tau_0^i - \tau_0}{\tau_0 - \tau_d}\left(1 - \sqrt{1 - 1/x^2}\right)\right] \quad (3)$$

where τ_0^i is initial shear stress inside the nucleation zone (Table 1). Using the values of parameters

Table 1. Fault Parameters

Fault Parameter	Value
Static friction coefficient, f_s	0.630
Dynamic friction coefficient, f_d	0.5
Effective normal stress, σ_n (MPa)	100
Initial shear stress, τ_0(MPa)	56
Initial shear stress (nucleation), τ_0^i (MPa)	63.4
Critical slip distance, d_0(m)	0.8
Domain (km^3)	$24 \times 40 \times 16$
Fault length (km)	36
Seismogenic depth (km)	3–10
Hypocenter depth (km)	6

Table 2. Minimum Elements Within the Cohesive Zone for Each Models[a]

	Depth Extent of LVFZs (km)									
Width (km)	1	2	3	4	5	6	7	8	9	10
0.4	9	9	10	8	5	6	4	4	4	4
0.8	9	9	9	8	4	4	3/4	3/4	3/4	3/4
1.6	9	9	9	5	*2*/5	*2*/5	3	*2*/4	**2**	**3**
2.4	9	9	8	5	*2*/4	*2*/4	**2**	**2**	**2**	**2**
3.2	9	9	8	5	*2*/4	**2**	**2**	**2**	**2**	**2**
4.0	9	9	9	4	*2*/4	**2**	**2**	**2**	**2**	**2**
4.8	9	9	8	4	*2*/4	**2**	**2**	**2**	**2**	**2**

[a]Italic numbers mark those models that do not have enough elements within the cohesive zone. Roman numbers behind the slash mark are those models with finer grids. Bold numbers mark those models that can rupture the entire fault.

listed in Table 1, F_{min} is ~1.58 and the critical nucleation size for an unbounded fault is ~2.7 km. Note that in our study the seismogenic zone is bounded in depth, i.e., 3–10 km. The critical nucleation size on bounded faults is larger than theoretical estimates on unbounded faults because stopping phases emit from the upper and lower fault edges and weaken rupture propagation [*Day*, 1982]. For instance, we have changed the sizes of nucleation zones for the depth-bounded fault and find that the critical nucleation zone is a rectangular patch of $16 \times 7\ km^2$ (i.e., the rupture can extend the entire fault), corresponding to a circular patch with radius of ~6 km. We set the radius of the circular nucleation zone as 3 km to ensure that the rupture does not propagate through the entire fault; and thus, we could investigate the effects of the LVFZ on the rupture extent.

For numerical rupture models, a good resolution at the rupture tip requires three or more elements within the cohesive zone [*Day et al.*, 2005]. The estimated static size of the cohesive zone for the slip-weakening law is

$$\Lambda_0 = \frac{9\pi}{32}\frac{\mu}{1-\nu}\frac{d_0}{\tau_s - \tau_d} \tag{4}$$

where Λ_0 is the static size of the cohesive zone. The grid size Δx is 200 m and the time step Δt is 0.005 s. Thus, $\Lambda_0/\Delta x \approx 11$ for the host rock and $\Lambda_0/\Delta x \approx 4$ for the smallest moduli of the LVFZ are both larger than the minimum requirement. We also measure the posteriori dynamic size of the cohesive zone for all the simulations (Table 2) and then rerun a few models with finer grids, e.g., 160 m or 100 m, until the numerical requirements are adequately satisfied. Here we use the seismic potency ($P_0 = uA$) to quantify the earthquake size, where A is the rupture area and u is the average fault slip [*Ben-Zion*, 2001].

4. Effects of LVFZ on Ruptures

We find that LVFZs can promote the rupture extents (Figures 2d and 2e). In the homogeneous model, rupture stops after propagating ~8 km along strike (Figure 2c). The corresponding seismic potency is $P_0 = \sim 1.06 \times 10^8\ m^3$. In comparison, the rupture propagates ~11 km along strike if there is a LVFZ with a depth extent of $d = 3$ km, a width of $w = 2.4$ km, and velocity reduction of $\Delta V = 40\%$ (Figure 2d). In this case the seismic potency is $P = \sim 1.58 \times 10^8\ m^3$, nearly 50% larger than that of the homogenous model. If the LVFZ extends deeper, e.g., $d = 5$ km, the rupture could extend to ~15 km along strike (Figure 2e), resulting in a seismic potency of $P = 2.33 \times 10^8\ m^3$, nearly 2.2 times that of the homogenous model.

4.1. Width Effects

To systematically investigate the effects of the LVFZ width on rupture propagation, we fix the depth extent of the LVFZ and only vary the width. Since we do not allow rupture propagation in depths shallower than 3 km, we first fix the depth extent of the LVFZ as 3 km, which serves as an end-member model. The width of the LVFZ is changed from 0.4 to 4.8 km.

We find that the seismic potency increases with the width of the LVFZ (Figures 3a and 3b). As the width increases from 0.4 km to 4.8 km, the normalized seismic potency (ratios between potencies for models with LVFZs and the model without LVFZ, P_0) increases almost linearly, from ~1.2 to ~1.8 (Figure 3b). The smallest width of the LVFZ in this study, i.e., 0.4 km, results in a seismic potency nearly 20% larger than that of the homogenous model (Figure 3b). There is an abrupt increase of seismic potency as the width of the LVFZ increases from 0 km to 0.4 km, and then the seismic potency increases almost linearly at a gradual slope from 0.4 km to 4.8 km.

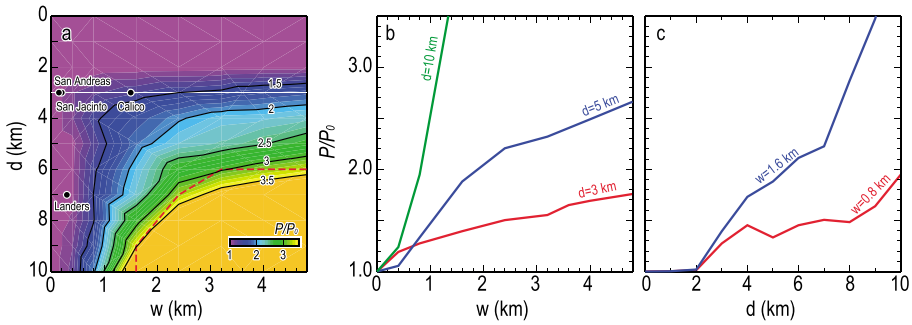

Figure 3. (a) A contour map of the normalized seismic potencies (ratios between potencies for models with LVFZs and the model without LVFZ, P_0) on the width and depth extent of the LVFZ. $\Delta V = 40\%$. Black circles mark the observations of LVFZs in California. White solid line indicates the depth extent of the aseismic region L_d. Red dash line indicates the boundary that the rupture extents are not limited by the fault boundaries. (b) Normalized seismic potency versus the width for different depth extents of the LVFZ. (c) Normalized seismic potency versus the depth extent for different widths of the LVFZ.

We consider another end-member model, a LVFZ with a depth extent of 10 km reaching the bottom of our seismogenic zone. The ruptures propagate entirely within the LVFZ, similar to a 2-D model [e.g., *Huang et al*., 2014]. We find that the seismic potency increases sharply with the width of the LVFZ (Figures 3a and 3b).

4.2. Depth Effects

In addition to the width, the depth extent also plays a significant role in promoting rupture propagation. In cases that we do not allow rupture propagation in depths shallower than 3 km, a very shallow LVFZ (e.g., 2 km in depth) has little effects on rupture propagation (Figures 3a and 3c). LVFZs promote the ruptures only when their bottom is close to the seismogenic zone, e.g., at less than 1 km distance.

When the LVFZ extends to greater depths, it may also promote the rupture extent so as to increase the seismic potency (Figures 3a and 3c). Figure 3c shows the seismic potency versus the depth extent of the LVFZ for $w = 0.8$ km and $w = 1.6$ km. From $d = 0$ km to $d = 2$ km, the seismic potency increases slowly, then more quickly from $d = 2$ km to $d = 4$ km. For larger depths, the seismic potency for $w = 0.8$ km becomes nearly independent of LVFZ depth, but for $w = 1.6$ km it still increases sharply.

The promotional effects on rupture propagation are dependent on both depth extent and width of the LVFZ. In our simulated cases, the LVFZs promote the ruptures when the width is larger than 200 m and the depth extent is greater than 2 km. Since we choose a rather small nucleation zone on the depth-bounded fault, only a few ruptures break the entire fault. The red dash line in Figure 3a separates two different cases: self-arrested and runaway ruptures (i.e., breaks the entire fault in this study).

For the self-arrested cases (left side of the red dash line in Figure 3a), the rupture extents are smaller than fault dimension, and the LVFZs promote both rupture extents and seismic potencies. When the depth extent of the LVFZ is larger than 6 km and the width of the LVFZ is larger than 1.6 km (the red dash line in Figure 3a), the ruptures propagate through the entire fault plane, forming large earthquakes whose potencies are at least 3.5 times than that of the model without LVFZ. For these cases, although the rupture extents are limited by the fault boundaries, we observe that the average slip and seismic potency still increase with the width of the LVFZ. For an extreme case with a LVFZ of infinite width, seismic potency is the largest among all the computed models.

4.3. Along-Strike Variations

Here we investigate how segmented LVFZs affect rupture propagation. First, we reduce the along-strike length of the LVFZ by half, while keeping one end of the LVFZ located at the center of the fault (Figure 4b). Other parameters of the LVFZ are $d = 5$ km, $w = 2.4$ km, and $\Delta V = 40\%$. We find that the rupture propagates a larger distance in the LVFZ side than in the side without LVFZ (Figure 4b), forming an asymmetric along-strike rupture pattern.

In addition, we further reduce the along-strike length of the LVFZ to a segmented LVFZ, e.g., 6 km in length along strike (Figure 4c). This LVFZ is located completely outside the nucleation zone (Figure 4c). We find that this segmented LVFZ can also promote the rupture, but less than the full-length and half-length LVFZs (Figure 4). The

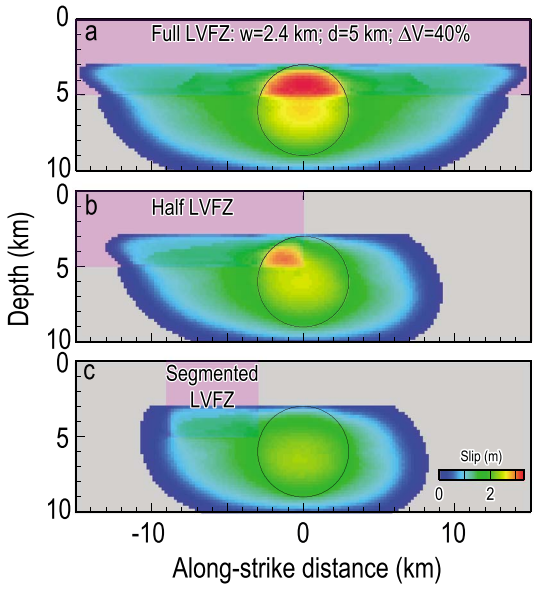

Figure 4. Slip distribution (color) for models with along-strike segmentations of the LVFZ. (a–c) The difference of the along-strike length of the LVFZ, shown as the pink rectangles. Circles mark the nucleation zone.

seismic potencies of the full-length, half-length, and segmented LVFZs in Figure 4 are $2.33\times10^8\,m^3$, $1.64\times10^8\,m^3$, and $1.35\times10^8\,m^3$, respectively.

4.4. Surface-Breaking Earthquakes

Since shallow LVFZs are usually interpreted as accumulative damages from surface-breaking earthquakes, we perform a few simulations allowing ruptures to propagate to the ground surface, i.e., seismogenic zone range is 0–10 km in depth. Given the 3 km radius nucleation patch, rupture can propagate through the entire fault. Thus, we reduce the radius to 2.6 km to investigate the effects of the LVFZ on the rupture extent. Rupture propagates out of the nucleation zone and then stops after a short distance (Figure 5a), resulting in a seismic potency of $P=0.72\times10^8\,m^3$.

We then implement a shallow LVFZ with $d=3$ km, $w=0.4$ km, and $\Delta V=40\%$ (Figure 5b). In addition to propagating further along strike, rupture is promoted in depths where the LVFZ extends (Figure 5b). The seismic potency for this model is $P=1.18\times10^8\,m^3$, 60% larger than that without LVFZ (Figure 5). If the LVFZ width is increased to $w=0.8$ km (Figure 5c), rupture then propagates along the entire fault, showing a stronger promotional effect.

4.5. Stress Perturbations Due To LVFZ Bottom

To investigate why shallow LVFZs (<3 km) promote rupture propagation, we compare shear stress fields within the seismogenic zone between the homogeneous model and the models with LVFZs. We subtract the shear stress field of the homogeneous model from that of the model with a LVFZ at the same time when only waves reflected from the LVFZ bottom may play roles, e.g., 1 s. In comparison, waves reflected from the free surface and side boundaries will propagate at an additional distance larger than $2\times L_d$, where $L_d=3$ km is the distance between the free surface and "the top" of the seismogenic zone (Figure 2). Thus, the shortest delayed time will be $2\times L_d/V_p=2\times3\,km/5.77\,km/s=1.04\,s$ for the largest P wave velocity of host rock; and therefore, these waves have minor effects on perturbing the shear stress field at the time we chose.

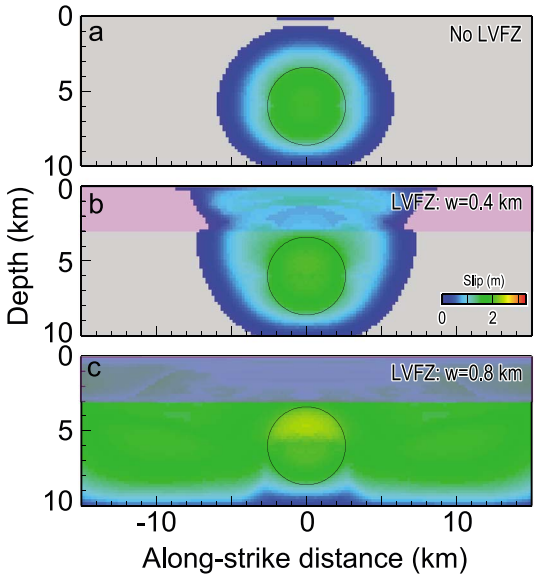

Figure 5. (a–c) Slip distribution (color) for the surface-breaking models, i.e., seismogenic zone range is 0–10 km in depth. The LVFZs are shown as the pink rectangles with $\Delta V=40\%$. The radius of the nucleation zone is 2.6 km for these cases.

We find that the waves reflected from the bottom of the shallow LVFZ could increase the shear stress outside the nucleation zone at the shallow fault (Figure 6a), making it easier to rupture. In addition, the LVFZ bottom-reflected waves decrease the shear stresses inside the nucleation zone. According to equation (1), smaller shear stress inside the nucleation zone means larger slip; and thus, the nucleation process is accelerated. Therefore, the bottom-reflected waves are favorable for promoting rupture propagation. Moreover, as the width of the LVFZ increases,

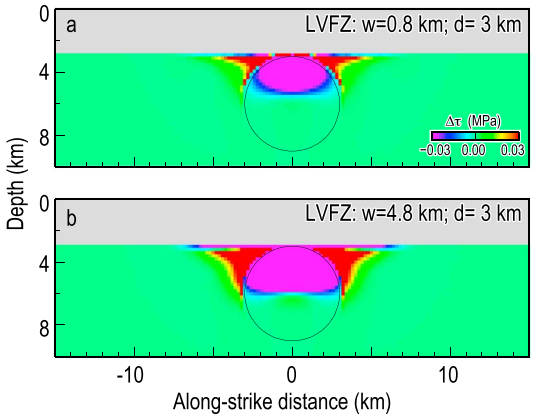

Figure 6. Residual shear stress at 1 s on the fault by subtracting the shear stress field of the homogeneous model from that of the model with a 3 km deep LVFZ. Circles mark the nucleation zones. (a) $w = 0.8$ km. (b) $w = 4.8$ km.

the excess loading from the bottom-reflected waves also increases (Figure 6b). In other words, a wider LVFZ could reflect more energy from the bottom to load the shallow fault and thus promote the rupture to extend larger.

5. Discussion

5.1. The Roles of Fault Zone Waves

If the depth of the LVFZ extends to the bottom of the seismogenic zone (i.e., 10 km in our models), the models are similar to 2-D models in which the ruptures completely propagate within the LVFZ [e.g., *Huang et al*., 2014]. It has been shown in 2-D models that the waves reflected from LVFZ side boundaries can induce multiple slip pulses and cause oscillations of rupture speed [*Huang et al*., 2014]. In particular, head waves that propagate along LVFZ side boundaries can accelerate the rupture speed and cause a permanent transition to supershear ruptures [*Huang et al*., 2016]. In our study, however, the rupture speeds are always lower than the *S* wave velocity of the LVFZ (e.g., Figure 7), in contrast to the supershear transition observed in 2-D simulations [*Huang et al*., 2014, 2016]. In their 2-D simulations [*Huang et al*., 2014, 2016], the supershear transition occurs for wider LVFZs (normalized widths) at a normalized distance longer than those in this study. In addition, the stopping phases emitting from the upper and lower fault edges may weaken the waves that could cause supershear ruptures in 2-D simulations.

As the effects of different fault zone waves have been shown in previous studies [*Huang et al*., 2014], we then do not duplicate the efforts to distinguish which phases may accelerate or decelerate ruptures. However, the overall effects of fault zone waves caused by side boundaries are unfavorable for rupture propagation. For instance, if comparing the two models with a LVFZ of 0.8 km and infinite width (i.e., without reflected waves and head waves), only part of the fault is ruptured in the former model while the entire fault is ruptured in the latter one (Figure 8). In addition, the rupture potency increases with the width of the LVFZ (Figure 3b), showing that the unfavorable effects of fault zone waves on rupture propagation weaken due to the geometrical spreading effects.

If the depth extents of LVFZs are shallower than the seismogenic zone, the LVFZs could also promote rupture propagation, as long as the LVFZs are close to the seismogenic zone (Figure 3a), due to the excess loading from LVFZ bottoms (Figure 6). Although LVFZs in the field may not always have sharp tabular bottoms [e.g., *Cochran et al*., 2009] as used in our models, the promotional effects of shallow LVFZs on rupture propagation may become smaller but will still exist. Since the LVFZs are widely identified in natural faults, the results may hold important implications for earthquake hazard assessment. Usually, the widths of the observed LVFZs of crustal faults range from ~100 m to ~1.5 km [e.g., *Yang*, 2015]. On the other hand, sedimentary basins could be regarded as "larger-scale low-velocity fault zones" with "infinite" width, which could extend several kilometers in depth [*Garfunkel and Ben-Avraham*, 1996]. Although shallow sedimentary basins may be aseismic due to the presence of the loosely consolidated materials [*Marone and Scholz*, 1988], they may have prominent effects on promoting ruptures that originate at seismogenic depths.

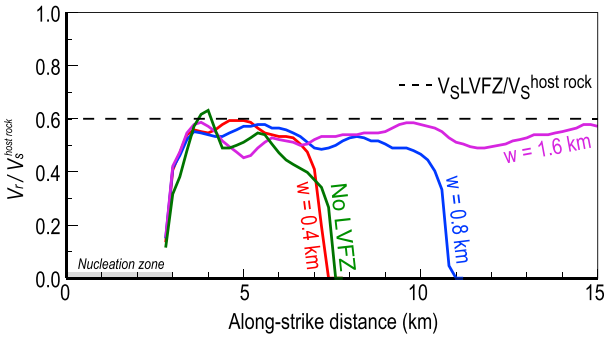

Figure 7. Rupture speeds at 6 km depth normalized with *S* wave velocity of host rock, $V_s^{host\ rock}$, for those models with $d = 10$ km and $\Delta V = 40\%$. V_s^{LVFZ} marks the *S* wave velocity of the LVFZ.

5.2. Segmentation of LVFZs

Along-strike variations of LVFZs have been documented at several faults, such as the SJF and SAF near Parkfield [*Yang et al*., 2014; *Lewis and Ben-Zion*, 2010]. In this

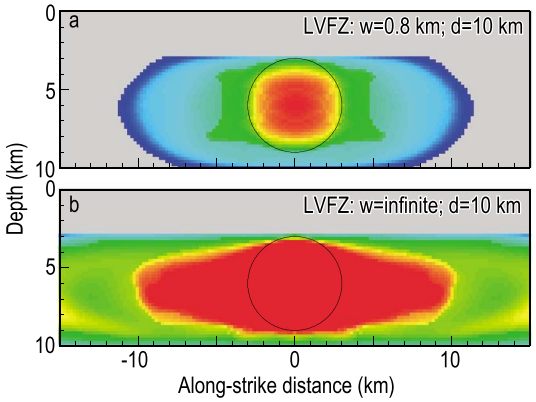

Figure 8. Slip distribution (color) for the models with different LVFZ widths (a) $w = 0.8$ km, (b) $w =$ infinite.

study, we find the along-strike segmented LVFZs could asymmetrically promote rupture propagation. If earthquake hypocenters are close to the segmented LVFZ, ruptures will propagate preferentially toward the LVFZ (Figure 4). The prediction of rupture directivity has a significant implication on assessing earthquake risk, since the rupture directivity effects may increase the ground motion damage and triggered seismicity toward the rupture direction [*Somerville et al.*, 1997; *Gomberg et al.*, 2001]. It has been suggested that the bimaterial interface effects may affect rupture directions considering homogeneous initial stress distribution [*Ampuero and Ben-Zion*, 2008]. If the initial stress on a bimaterial fault is sufficiently heterogeneous, there is no preferred rupture direction [*Ampuero and Ben-Zion*, 2008]. Similarly, the bimaterial effect becomes insignificant if a length scale for normal-stress regularization is chosen similar to the critical slip-weakening distance [e.g., *Harris and Day*, 2005]. Here we show one possibility that along-strike variations of LVFZs may induce unilateral ruptures if earthquake hypocenters are near the LVFZ and other stress/friction properties on fault are uniform (Figure 4b).

In addition, along-strike segmentation of LVFZs may provide a natural laboratory to observe the promotional effects of LVFZs in field. If a fault has been documented with well-defined segmented LVFZs and has uniform frictional properties, long-term observations of seismicity might show along-strike variation of statistical features such as Gutenberg-Richter law and accumulated moment. This requires high-resolution near-fault seismic observations and could be a future work at a suitable site to observe such promotional effects.

5.3. Effective Shear Modulus

Here we use seismic potency because it has been suggested as a proper physical measure for the size of an earthquake without assuming material properties near the source [*Ben-Zion*, 2001]. This is especially convenient for those cases that occurred on a bimaterial fault interface. To calculate seismic moments for our simulated earthquakes, it may be more suitable to use the concept of effective shear modulus for the bulk material with LVFZs [*Capdeville et al.*, 2010a, 2010b]. There are two end-member cases: an infinitely wide LVFZ with the shear modulus of the LVFZ (lower bound of shear modulus) and an extremely thin LVFZ with the host rock modulus (upper bound of shear modulus). Thus, the effective shear modulus apparently decreases with the increased depth and width of the LVFZ.

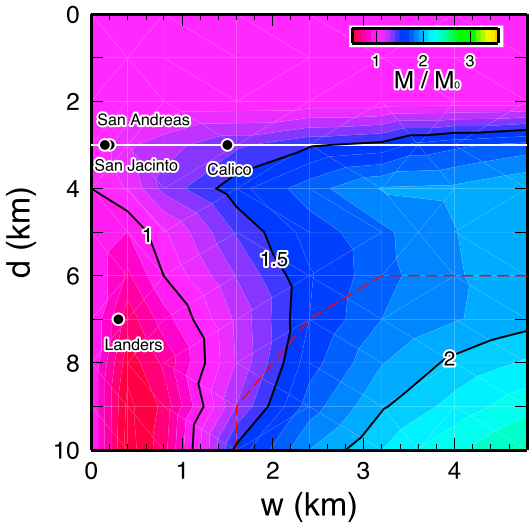

Figure 9. A contour map of the normalized seismic moments (ratios between moments for models with LVFZs and the model without LVFZ, M_0) on the width and depth extent of the LVFZ. Others are same as in Figure 3a.

The concept of effective shear modulus could help explain the promotional effects of the LVFZs. For the self-arrested cases, ruptures are promoted primarily because decreasing the critical nucleation size is proportional to the effective shear modulus (equation (2)). These cases could apply to noncharacteristic earthquakes (i.e., events do not break the entire fault), such as earthquakes induced by localized stresses at the boundaries between locked and creeping fault areas or by fluid injection. However, these cases may not apply to all noncharacteristic earthquakes in the nature since the self-arrested ruptures tend to have low radiation efficiency. For the runaway cases, the rupture extents are

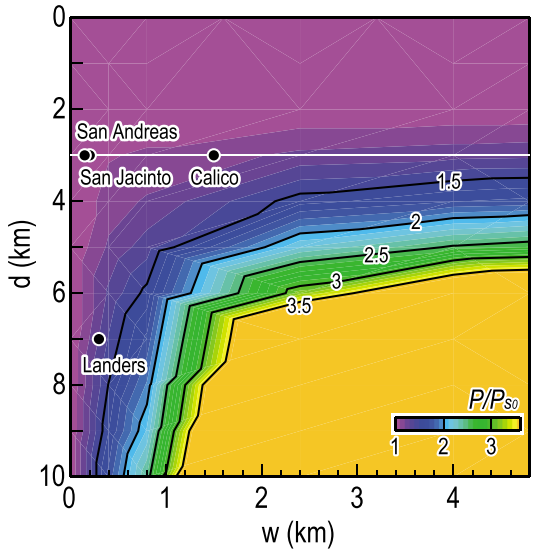

Figure 10. Same as Figure 3a except for a smoother nucleation procedure. The seismic potencies are normalized using P_{s0}.

limited by the fault boundaries in this study. The promoted seismic potencies can be explained by the following equation [e.g., *Aki*, 1972]:

$$u \propto \Delta\sigma L/\mu_{\text{eff}} \tag{5}$$

where u is average slip, $\Delta\sigma$ is average stress drop, L is rupture length, and μ_{eff} is effective shear modulus. Decreasing the effective shear modulus shall increase the average slip and thus seismic potency given the same rupture extent and stress drop. These cases could apply to characteristic earthquakes, as those in earthquake cycle simulations with a LVFZ and spontaneous nucleation [e.g., *Kaneko et al.*, 2011].

Here we calculate the lower bound of seismic moment ($M = \mu P$), using the shear modulus of LVFZs for the region inside the LVFZs regardless of the widths. The normalized seismic moment, ratios between moments for models with and without LVFZs, shows the same trend with the normalized seismic potency for shallow LVFZs, e.g., <4 km (Figures 9 and 3a). For deeper LVFZs, the seismic moment still increases with the width of the LVFZ. Note that the seismic moment decreases from $w = 0$ km to $w = 0.4$ km for deeper LVFZs (Figure 9), because we used the shear modulus of LVFZs. As the effective shear modulus for narrow LVFZs shall be closer to the shear modulus of host rock, rather than that of the LVFZ; thus, the moments are largely underestimated for those cases with narrow and deep LVFZs. This is another reason for us to use the seismic potency.

5.4. The Effects of Different Nucleation Procedures

It has been noted that the nucleation processes can affect rupture propagation [e.g., *Bizzarri*, 2010]. We employ a smoother nucleation procedure to initiate ruptures by forcing a constant rupture speed (half of S wave speed) using a finite difference code [*Zhang et al.*, 2014]. The fixed radius of the enforcing nucleation patch is 5 km to ensure that the rupture does not propagate through the entire fault. We apply a time-weakening friction law within the nucleation patch. Outside the nucleation zone, the fault is still governed by the slip-weakening law (Table 1). The seismic potency of the homogeneous model with smooth nucleation process is $P_{s0} = \sim 0.587 \times 10^8\ \text{m}^3$, less than that of the abrupt nucleation, $P_0 = \sim 1.06 \times 10^8\ \text{m}^3$. This is because the smooth nucleation process does not involve artificially additional shear stress. Although the numeric values of seismic potencies are affected by the nucleation process, the promotional effects on rupture propagation by the LVFZs are not changed (Figure 10).

We also employ the time-weakening procedure without prescribed maximum radius introduced by *Andrews* [1985] and determine the critical boundaries from time-weakening to slip-weakening friction (Figure 11). In all cases the nucleation evolves into slip weakening when the slip-weakening friction coefficient becomes smaller than the time-weakening coefficient. Since we used depth-bounded seismogenic fault, the critical boundaries are not ellipses. The critical transition distance is shortest at the intermediate depth of the fault.

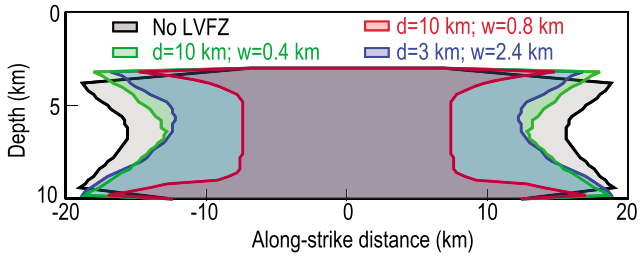

Figure 11. Critical boundaries from time-weakening friction to slip-weakening friction. $\Delta V = 40\%$ for the LVFZs.

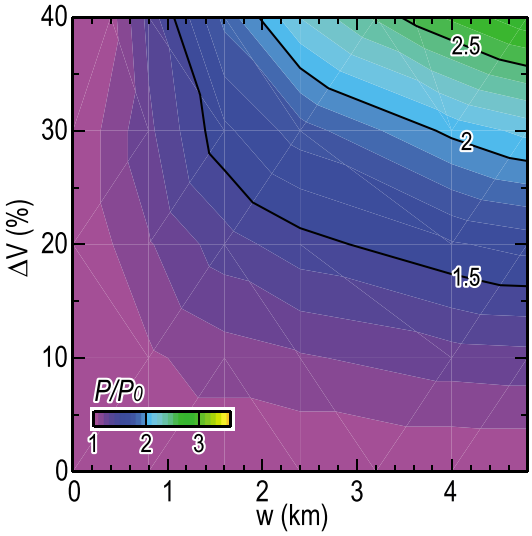

Figure 12. Dependence of normalized seismic potencies on the width and velocity reduction of the LVFZ. The depth of the LVFZ is fixed as 5 km. Others are the same as in Figure 3a.

Furthermore, the transition distance decreases with the increased width and depth of the LVFZ, which is consistent with other studies that LVFZs could reduce the "critical radius" of the nucleation zone [*Ampuero et al.*, 2002; *Kaneko et al.*, 2011]. Moreover, the critical size of nucleation zone for this bounded fault is much larger than the theoretical estimate of unbounded fault. Even though the rupture extends the entire fault (Figure 3a), seismic potency still increases as the width and depth of the LVFZ increase. Thus, we believe that our conclusion is not affected by different nucleation procedures.

5.5. Dependency on Velocity Reduction and *S* Ratio

We note that there is a trade-off between the width and velocity reduction of the LVFZ for the promotional effects (Figure 12). For instance, the model with a LVFZ of velocity reduction 40% and a width of 0.8 km could produce seismic potency similar to that of velocity reduction 10% and a width of 4 km (Figure 12). In other words, the promotional effects of the LVFZ will increase as velocity reduction increases. The largest value of velocity reduction in natural faults could reach as high as 60% [e.g., *Li et al.*, 2007], which may have stronger promotional effects, given the identical width and depth extent of the LVFZ.

In addition, initial stresses and frictional parameters play significant roles in rupture propagation [e.g., *Yang et al.*, 2012; *Weng et al.*, 2015]. For instance, it is well known that the *S* values (seismic ratio) can control rupture speed transition from subshear to supershear. Here we have tested the effects of *S* values on promoting rupture propagation (Figure 13). We find that the seismic potency increases with the width and depth of the LVFZ regardless the variation of *S* values. Thus, promotion of rupture propagation due to LVFZs does not change, given different initial stress distributions.

5.6. Factors Not Considered

In our numerical experiments, we have not considered the effects of inelasticity within the fault zone [e.g., *Huang et al.*, 2014], geometrical roughness on the fault [e.g., *Yang et al.*, 2013], and fluid effects [e.g., *Liu*, 2013]. For instance, the damaged plastic materials may attenuate the seismic waves and thus cause a trade-off between the estimations of fault zone width, velocity, and *Q* [*Ben-Zion*, 1998]. In addition, irregular

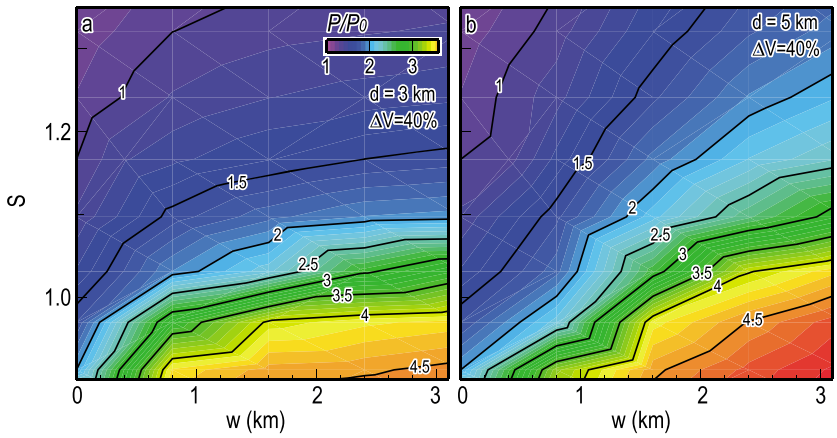

Figure 13. Dependence of normalized seismic potency on *S* value, the width and depth of the LVFZ.

geometrical patches on the fault could stop the ruptures and thus may quantitatively affect the rupture extents [*Yang et al*., 2013]. Moreover, the local stress field inside a fault zone may be different than those of the host rock, including the magnitude and the directions of the principal stresses [*Gudmundsson et al*., 2010]. The state of stress may organize in a nontrivial way throughout multiple earthquake cycles and can differ from the uniform initial stress assumption significantly [*Kaneko et al*., 2011]. Although these ignored factors may probably change the numeric values of the rupture extents and the seismic potencies, our main conclusions of the promotional effects of the LVFZ on rupture will still hold qualitatively.

6. Conclusions

Our numerical results show that LVFZs can promote coseismic rupture propagation and thus increase seismic potencies, in addition to well-studied amplification effects on ground motions [e.g., *Ben-Zion and Aki*, 1990]. The promotional effects of the LVFZ increase with its width and depth extent. When the entire fault is broken, i.e., under supercritical nucleation condition [e.g., *Galis et al*., 2015; *Andrews*, 1985], LVFZs can still promote average slip and thus the seismic potency. Moreover, along-strike segmentations of the LVFZ could also promote rupture propagation and may induce unilateral ruptures, providing a plausible mechanism to the preferred rupture directions. High-resolution imaging of the properties of LVFZs and sedimentary basins, as well as numerical simulations of ground motion and dynamic ruptures, is highly demanded to better assess earthquake risk.

Acknowledgments

H. Weng and H. Yang are supported by Yang's startup fund (grant 4930072) and Direct Grant for Research (grants 4053114 and 3132771) from Chinese University of Hong Kong, as well as Research Grant Council (grant 2191093). This work is also supported by National Natural Science Foundation of China (grants 41274053 and 41504040). All data used in this study are generated from numerical simulations and available by contacting the corresponding author at hyang@cuhk.edu.hk. All figures are produced using Generic Mapping Tools (GMT). The authors thank Fan Zhang for helping refine all figures. The authors appreciate the constructive comments on the effective shear modulus and nucleation process provided by the Editor, the Associate Editor Jean-Paul Ampuero, Yihe Huang, and an anonymous reviewer that substantially improve the paper.

References

Aagaard, B., M. Knepley, and C. Williams (2013), A domain decomposition approach to implementing fault slip in finite-element models of quasi-static and dynamic crustal deformation, *J. Geophys. Res. Solid Earth*, *118*, 3059–3079, doi:10.1002/jgrb.50217.

Aki, K. (1972), Earthquake mechanism, *Tectonophysics*, *13*(1–4), 423–446.

Allam, A., Y. Ben-Zion, I. Kurzon, and F. Vernon (2014), Seismic velocity structure in the Hot Springs and Trifurcation areas of the San Jacinto Fault zone, California, from double-difference tomography, *Geophys. J. Int.*, *198*, 978–999.

Ampuero, J. P., J. P. Vilotte, and F. Sanchez-Sesma (2002), Nucleation of rupture under slip dependent friction law: Simple models of fault zone, *J. Geophys. Res.*, *107*(B12), 2324, doi:10.1029/2001JB000452

Ampuero, J.-P., and Y. Ben-Zion (2008), Cracks, pulses and macroscopic asymmetry of dynamic rupture on a bimaterial interface with velocity-weakening friction, *Geophys. J. Int.*, *173*, 674–692.

Andrews, D. (1985), Dynamic plane-strain shear rupture with a slip-weakening friction law calculated by a boundary integral method, *Bull. Seismol. Soc. Am.*, *75*(1), 1–21.

Ben-Zion, Y. (1998), Properties of seismic fault zone waves and their utility for imaging low-velocity structures, *J. Geophys. Res.*, *103*(B6), 12,567–12,585, doi:10.1029/98JB00768.

Ben-Zion, Y. (2001), On quantification of the earthquake source, *Seismol. Res. Lett.*, *72*, 151–152.

Ben-Zion, Y., and C. G. Sammis (2003), Characterization of fault zones, *Pure Appl. Geophys.*, *160*, 677–715.

Ben-Zion, Y., and K. Aki (1990), Seismic radiation from an SH line source in a laterally heterogeneous planar fault zone, *Bull. Seismol. Soc. Am.*, *80*, 971–994.

Ben-Zion, Y., and Y. Huang (2002), Dynamic rupture on an interface between a compliant fault zone layer and a stiffer surrounding solid, *J. Geophys. Res.*, *107*(B2), 2042, doi:10.1029/2001JB000254.

Ben-Zion, Y., Z. Peng, D. Okaya, L. Seeber, J. G. Armbruster, N. Ozer, A. J. Michael, S. Baris, and M. Aktar (2003), A shallow fault-zone structure illuminated by trapped waves in the Karadere-Duzce branch of the North Anatolian Fault, western Turkey, *Geophys. J. Int.*, *152*, 699–717.

Bizzarri, A. (2010), How to promote earthquake ruptures: Different nucleation strategies in a dynamic model with slip-weakening friction, *Bull. Seismol. Soc. Am.*, *100*, 923–940.

Brietzke, G. B., and Y. Ben-Zion (2006), Examining tendencies of in-plane rupture to migrate to material interfaces, *Geophys. J. Int.*, *167*, 807–819.

Capdeville, Y., L. Guillot, and J.-J. Marigo (2010a), 1-D non-periodic homogenization for the seismic wave equation, *Geophys. J. Int.*, *181*, 897–910.

Capdeville, Y., L. Guillot, and J.-J. Marigo (2010b), 2-D non-periodic homogenization to upscale elastic media for P-SV waves, *Geophys. J. Int.*, *182*, 903–922.

Cappa, F., C. Perrin, I. Manighetti, and E. Delor (2014), Off-fault long-term damage: A condition to account for generic, triangular earthquake slip profiles, *Geochem. Geophys. Geosyst.*, *15*, 1476–1493, doi:10.1002/2013GC005182.

Cochran, E. S., Y.-G. Li, P. M. Shearer, S. Barbot, Y. Fialko, and J. E. Vidale (2009), Seismic and geodetic evidence for extensive, long-lived fault damage zones, *Geology*, *37*, 315–318.

Day, S. M. (1982), Three-dimensional finite difference simulation of fault dynamics: Rectangular faults with fixed rupture velocity, *Bull. Seismol. Soc. Am.*, *72*, 705–727.

Day, S. M., L. A. Dalguer, N. Lapusta, and Y. Liu (2005), Comparison of finite difference and boundary integral solutions to three-dimensional spontaneous rupture, *J. Geophys. Res.*, *110*, B12307, doi:10.1029/2005JB003813.

Dor, O., T. K. Rockwell, and Y. Ben-Zion (2006), Geological observations of damage asymmetry in the structure of the San Jacinto, San Andreas and Punchbowl faults in Southern California: A possible indicator for preferred rupture propagation direction, *Pure Appl. Geophys.*, *163*, 301–349.

Fialko, Y. (2004), Probing the mechanical properties of seismically active crust with space geodesy: Study of the coseismic deformation due to the 1992 M_w7.3 Landers (Southern California) earthquake, *J. Geophys. Res.*, *109*, B03307, doi:10.1029/2003JB002756.

Galis, M., C. Pelties, J. Kristek, P. Moczo, J.-P. Ampuero, and P. M. Mai (2015), On the initiation of sustained slip-weakening ruptures by localized stresses, *Geophys. J. Int.*, *200*, 890–909, doi:10.1093/gji/ggu436.

Garfunkel, Z., and Z. Ben-Avraham (1996), The structure of the Dead Sea basin, *Tectonophysics*, *266*, 155–176.

Gomberg, J., P. Reasenberg, P. Bodin, and R. Harris (2001), Earthquake triggering by seismic waves following the Landers and Hector Mine earthquakes, *Nature*, *411*, 462–466.

Gudmundsson, A., T. H. Simmenes, B. Larsen, and S. L. Philipp (2010), Effects of internal structure and local stresses on fracture propagation, deflection, and arrest in fault zones, *J. Struct. Geol.*, *32*, 1643–1655.
Harris, R. A., and S. M. Day (1997), Effects of a low-velocity zone on a dynamic rupture, *Bull. Seismol. Soc. Am.*, *87*, 1267–1280.
Harris, R. A., and S. M. Day (2005), Material contrast does not predict earthquake rupture propagation direction, *Geophys. Res. Lett.*, *32*, L23301, doi:10.1029/2005GL023941.
Hillers, G., M. Campillo, Y. Ben-Zion, and P. Roux (2014), Seismic fault zone trapped noise, *J. Geophys. Res. Solid Earth*, *119*, 5786–5799, doi:10.1002/2014JB011217.
Huang, Y., and J. P. Ampuero (2011), Pulse-like ruptures induced by low-velocity fault zones, *J. Geophys. Res.*, *116*, B12307, doi:10.1029/2011JB008684.
Huang, Y., J. P. Ampuero, and D. V. Helmberger (2014), Earthquake ruptures modulated by waves in damaged fault zones, *J. Geophys. Res. Solid Earth*, *119*, 3133–3154, doi:10.1002/2013JB010724.
Huang, Y., J. P. Ampuero, and D. V. Helmberger (2016), The potential for supershear earthquakes in damaged fault zones-theory and observations, *Earth Planet. Sci. Lett.*, *433*, 109–115, doi:10.1029/2001JB000452.
Ida, Y. (1972), Cohesive force across the tip of a longitudinal-shear crack and Griffith's specific surface energy, *J. Geophys. Res.*, *77*, 3796–3805, doi:10.1029/JB077i020p03796.
Kaneko, Y., J. P. Ampuero, and N. Lapusta (2011), Spectral-element simulations of long-term fault slip: Effect of low-rigidity layers on earthquake-cycle dynamics, *J. Geophys. Res.*, *116*, B10313, doi:10.1029/2011JB008395
Kang, J., and B. Duan (2015), Elastic and inelastic responses of compliant fault zones to nearby earthquakes in three dimensions: A parameter-space study, *Geophys. J. Int.*, *201*, 1195–1214.
Lewis, M. A., and Y. Ben-Zion (2010), Diversity of fault zone damage and trapping structures in the Parkfield section of the San Andreas fault from comprehensive analysis of near fault seismograms, *Geophys. J. Int.*, *183*, 1579–1595.
Lewis, M., Z. Peng, Y. Ben-Zion, and F. Vernon (2005), Shallow seismic trapping structure in the San Jacinto fault zone near Anza, California, *Geophys. J. Int.*, *162*, 867–881.
Li, H., L. Zhu, and H. Yang (2007), High-resolution structures of the Landers fault zone inferred from aftershock waveform data, *Geophys. J. Int.*, *171*, 1295–1307.
Li, Y. G., and F. L. Vernon (2001), Characterization of the San Jacinto fault zone near Anza, California, by fault zone trapped waves, *J. Geophys. Res.*, *106*, 30,671–30,688, doi:10.1029/2000JB000107.
Li, Y. G., K. Aki, D. Adams, A. Hasemi, and W. H. Lee (1994), Seismic guided waves trapped in the fault zone of the Landers, California, earthquake of 1992, *J. Geophys. Res.*, *99*, 11,705–11,722, doi:10.1029/94JB00464.
Li, Y. G., J. E. Vidale, S. M. Day, D. D. Oglesby, and S. F. W. Team (2002), Study of the 1999 M 7.1 Hector Mine, California, earthquake fault plane by trapped waves, *Bull. Seismol. Soc. Am.*, *92*, 1318–1332.
Lindsey, E. O., V. J. Sahakian, Y. Fialko, Y. Bock, S. Barbot, and T. K. Rockwell (2014), Interseismic strain localization in the San Jacinto fault zone, *Pure Appl. Geophys.*, *171*, 2937–2954.
Liu, Y. (2013), Numerical simulations on megathrust rupture stabilized under strong dilatancy strengthening in slow slip region, *Geophys. Res. Lett.*, *40*, 1311–1316, doi:10.1002/grl.50298.
Ma, X., and A. Elbanna (2015), Effect of off-fault low-velocity elastic inclusions on supershear rupture dynamics, *Geophys. J. Int.*, *203*(1), 664–677, doi:10.1093/gji/ggv302.
Marone, C., and C. Scholz (1988), The depth of seismic faulting and the upper transition from stable to unstable slip regimes, *Geophys. Res. Lett.*, *15*, 621–624, doi:10.1029/GL015i006p00621.
Mizuno, T., Y. Kuwahara, H. Ito, and K. Y. Nishigami (2008), Spatial variations in fault-zone structure along the Nojima fault, central Japan, as inferred from borehole observations of fault-zone trapped waves, *Bull. Seismol. Soc. Am.*, *98*, 558–570.
Pelties, C., Y. Huang, and J.-P. Ampuero (2015), Pulse-like rupture induced by three-dimensional fault zone flower structures, *Pure Appl. Geophys.*, *172*, 1229–1241.
Peng, Z., Y. Ben-Zion, A. J. Michael, and L. Zhu (2003), Quantitative analysis of seismic fault zone waves in the rupture zone of the 1992 Landers, California, earthquake: Evidence for a shallow trapping structure, *Geophys. J. Int.*, *155*, 1021–1041.
Somerville, P. G., N. F. Smith, R. W. Graves, and N. A. Abrahamson (1997), Modification of empirical strong ground motion attenuation relations to include the amplitude and duration effects of rupture directivity, *Seismol. Res. Lett.*, *68*, 199–222.
Stierman, D. J. (1984), Geophysical and geological evidence for fracturing, water circulation and chemical alteration in granitic rocks adjacent to major strike-slip faults, *J. Geophys. Res.*, *89*, 5849–5857, doi:10.1029/JB089iB07p05849.
Wdowinski, S. (2009), Deep creep as a cause for the excess seismicity along the San Jacinto fault, *Nat. Geosci.*, *2*, 882–885.
Weng, H., J. Huang, and H. Yang (2015), Barrier-induced supershear ruptures on a slip-weakening fault, *Geophys. Res. Lett.*, *42*, 4824–4832, doi:10.1002/2015GL064281.
Wu, J., J. A. Hole, and J. A. Snoke (2010), Fault zone structure at depth from differential dispersion of seismic guided waves: Evidence for a deep waveguide on the San Andreas Fault, *Geophys. J. Int.*, *182*, 343–354.
Xu, J., H. Zhang, and X. Chen (2015), Rupture phase diagrams for a planar fault in 3-D full-space and half-space, *Geophys. J. Int.*, *202*, 2194–2206.
Yang, H. (2015), Recent advances in imaging crustal fault zones: A review, *Earthq. Sci.*, *28*, 151–162.
Yang, H., and L. Zhu (2010), Shallow low-velocity zone of the San Jacinto fault from local earthquake waveform modelling, *Geophys. J. Int.*, *183*, 421–432.
Yang, H., L. Zhu, and E. S. Cochran (2011), Seismic structures of the Calico fault zone inferred from local earthquake travel time modelling, *Geophys. J. Int.*, *186*, 760–770.
Yang, H., Y. Liu, and J. Lin (2012), Effects of subducted seamounts on megathrust earthquake nucleation and rupture propagation, *Geophys. Res. Lett.*, *39*, L24302, doi:10.1029/2012GL053892.
Yang, H., Y. Liu, and J. Lin (2013), Geometrical effects of a subducted seamount on stopping megathrust ruptures, *Geophys. Res. Lett.*, *40*, 2011–2016, doi:10.1002/grl.50509.
Yang, H., Z. Li, Z. Peng, Y. Ben-Zion, and F. Vernon (2014), Low-velocity zones along the San Jacinto Fault, Southern California, from body waves recorded in dense linear arrays, *J. Geophys. Res. Solid Earth*, *119*, 8976–8990, doi:10.1002/2014JB011548.
Zhang, Z., W. Zhang, and X. Chen (2014), Three-dimensional curved grid finite-difference modelling for non-planar rupture dynamics, *Geophys. J. Int.*, *199*, 860–879.